

1 Deep crustal architecture of the Parnaíba basin of
2 NE Brazil from receiver function analysis:
3 Implications for basin subsidence.

4 Diogo L.O. Coelho^{1,*}, Jordi Julià^{1,2}, Verónica Rodríguez-Tribaldos³, Nicholas

5 White³

6 ¹*Programa de Pós-graduação em Geodinâmica e Geofísica, Universidade Federal do Rio
7 Grande do Norte, Lagoa Nova, Natal-RN, CEP 59078-970, Brazil*

8 ²*Departamento de Geofísica, Universidade Federal do Rio Grande do Norte, Lagoa Nova,
9 Natal-RN, CEP 59078-970, Brazil*

10 ³*Bullard Laboratories, Department of Earth Sciences, University of Cambridge, Madingley
11 Rise House, Madingley Road, Cambridge, CB3 0EZ, UK*

12 *Corresponding author (e-mail: locdiogo@gmail.com)

13 **Abstract**

14 We investigate the crustal architecture of the Parnaíba basin of NE Brazil by analyzing
15 receiver functions along a ~600 km-long transect crossing the central portion of the basin.
16 The transect consisted of 9 broadband stations interspaced at ~70 km distance and record-
17 ing continuously for a period of 15 months, with the goal of improving our understanding of
18 the origin and evolution of this large cratonic basin. Our results reveal that crustal thickness
19 varies between 39 and 45 km along the transect, gradually thickening towards the depocen-
20 ter, and that bulk Vp/Vs ratios vary between 1.70 and 1.78. The crust can be generally
21 divided into a 2.0-3.5 km thick layer of low-velocity sediments, a 15-20 km thick upper crust
22 with S-velocities around 3.5-3.6 km/s, and a 18-22 km thick lower crust with S-velocities
23 around 3.7-3.8 km/s. Near the depocenter, where the crust is thickest, the bottom 10-12

24 km of the crust are characterized by fast S-velocities around 4.0-4.2 km/s. The crust-mantle
25 boundary is generally gradational, and reaches typical upper mantle S-velocities of 4.5-4.6
26 km/s. Our findings confirm that stretching of the lithosphere must be minimal - as indepen-
27 dently suggested by seismic profiling, gravity modeling, and surface geology - and are found
28 compatible with models invoking flexural subsidence driven by a deep, buried load. However,
29 loading from a thick, high-density layer of mafic intrusives pervading the lower crust - as re-
30 cently proposed for the basin - is found inconsistent with bulk Vp/Vs ratios and lower crustal
31 velocities from our S-velocity models. Flexural bending by a deeper load, perhaps related
32 to convecting processes in the underlying asthenosphere, seems more plausible, but need to
33 be investigated further in order to fully assess the origin and evolution of the Parnaíba basin.

34

35 **Keywords:** Cratonic subsidence, Basement architecture, South America

36

37 Introduction

38 The genesis and evolution of large basins in the stable interiors of continents is an impor-
39 tant geological problem that is not easily understood within the Plate Tectonics paradigm.
40 In spite of notable attempts by *Klein and Hsui (1987)* to link the formation of all cratonic
41 basins of Europe, Africa, North and South America to rifting and break-up of a Late Pre-
42 cambrian supercontinent, no single mechanism seems capable of explaining the development
43 of cratonic basins on such a large scale. This inability is nicely illustrated in *Kaminski and*
44 *Jaupart (2000)*, who showed that in spite of the four major cratonic basins of North America
45 - Hudson Bay, Michigan, Illinois, and Williston - having similar ages and being close to one
46 another, they exhibit different subsidence histories and are characterized by different time-

47 scales and sediment thicknesses. Adding to this complexity, is the intriguing observation
48 that prolonged intervals of slow subsidence alternate with fast subsidence rates (*Cloetingh*
49 *and Burov, 2011*). Although periods of fast subsidence often coincide with orogenic activity
50 at plate boundaries, the impression remains that individual mechanisms might be needed
51 to understand the large variety of depositional histories in cratonic basins worldwide.

52 The Parnaíba basin of NE Brazil is one of three large Paleozoic basins in stable South
53 America - together with the Paraná basin of SE Brazil and the Amazon basin, in the northern
54 half of the continent. The basin is commonly described as a large, sag-type cratonic basin,
55 with a roughly circular shape and a depocenter reaching up to 3.5 km depth (*Góes and Feijó,*
56 *1994; Vaz et al., 2007; Daly et al., 2014*). It is generally agreed that initial subsidence of the
57 basin occurred in an intra-continental setting during Paleozoic times, with the proto-basin
58 being framed by three large cratonic masses (Figure 1): Amazon to the West, São Luiz-West
59 Africa to the North, and São Francisco-Congo to the South and East (*Almeida et al., 1981;*
60 *Brito Neves et al., 1984; Cordani et al., 2009; Brito Neves and Fuck, 2013; Cordani et al.,*
61 *2013*). The physical mechanism behind its subsidence and evolution, on the other hand,
62 is more controversial. A number of basin-forming mechanisms have been proposed for this
63 basin, which fall into one of the following broad categories: (i) Thermally-driven subsidence,
64 which is based on a number of seismically identified unconformities in the sedimentary record
65 of the basin combined with evidence lacking for rifting structures (*Daly et al., 2014*); (ii)
66 thermo-mechanical subsidence, which relies on the inference of graben-like structures in the
67 basin's basement from interpreted gravity, magnetic, and pseudo-gravity residual anomalies
68 (*Brito Neves et al., 1984; Nunes, 1993; Cordani et al., 1984; de Castro et al., 2014*); and
69 (iii) flexural subsidence, driven by the load of a high-density, intrusive body in the lower
70 crust, postulated from modeling of gravity anomalies (*Tozer et al., 2017*).

Very little is known about the deep, crustal architecture of this enigmatic cratonic basin. Most of our current knowledge is restricted to low-resolution, continental-scale studies (*Feng et al., 2004; 2007; Lloyd et al., 2010; van der Meijde et al., 2013; Assumpção et al., 2013a; 2013b; Uieda and Barbosa, 2017*), a single seismic reflection line crossing the basin in the EW direction (*Daly et al., 2014*), and a colocated gravity survey along the same EW-trending line (*Tozer et al., 2017*). Continental-scale studies showed the crust is thinnest (30-35 km) under the Proterozoic provinces of South America, while thickest under cratonic landmasses (e.g. Amazon and São Francisco, 41 ± 4 km) and cratonic basins (e.g. Paraná and Parnaíba, 42 ± 4 km). More detailed information was developed from the seismic reflection survey of *Daly et al. (2014)*, where a basin-wide migrated cross-section demonstrated the presence of up to three different crustal blocks under the basin: a 35-44 km thick, highly reflective crustal block to the East, interpreted as the continuation of the Proterozoic Borborema Province; a ~ 40 km thick, moderately reflective crustal block to the West, identified as the Amazon craton; and a central, almost transparent crustal block referred to as the Parnaíba block with a locally defined Moho at about 38 km depth. Surprisingly, no crustal thickness estimates were reported for most of the central Parnaíba block, as the reflection signature expected from the crust-mantle boundary seemed to be absent in the migrated cross section. Most recently, seismic and gravity modeling along a profile coincident with the seismic reflection line has revealed a two-layer crust for the Parnaíba block, with an upper-lower crustal boundary at 17-25 km depth and a relatively flat Moho at $\sim 42 \pm 2$ km depth (*Tozer et al., 2017*).

In this work, we characterize the deep, crustal architecture of the Parnaíba basin by mapping subsurface seismic discontinuities with teleseismic P-wave receiver functions (*Langston, 1979*). We present point estimates of crustal thickness and Vp/Vs ratio at 9 broadband sta-

tions developed through the H κ -stacking procedure of *Zhu and Kanamori (2000)*, along with detailed S-wave velocity-depth profiles obtained from the joint inversion of receiver functions and surface-wave dispersion velocities (*Julia et al., 2000; 2003*). The H κ -stacking analysis reveals the crust could be as thick as 44-45 km around the basin's depocenter and that it progressively thins to 39-41 km towards de edges, while bulk Vp/Vs ratios are in the 1.70-1.78 range along the transect, with larger values around the depocenter. The velocity-depth profiles confirm crustal thickness variations from the H κ -stacking analysis and additionally reveal a lower crustal layer below 18-22 km depth, with S-velocities in the 3.7-3.8 km/s range that locally raise to 4.0-4.2 km/s near the depocenter. Our findings favor models invoking minimal stretching of the basin's underlying crust and are found compatible with flexural bending by a deep load. However, the existence of a thick, intrusive body pervading the lower crust is not supported by our results. We argue that deep convecting processes in the asthenosphere might provide an alternative loading mechanism.

Geology and Tectonic Setting

The depositional history of the Parnaíba basin is built on five primary tectono-sedimentary sequences and two magmatic pulses separated by regional unconformities (*Góes and Feijó, 1994; Vaz et al., 2007*). Following *Tozer et al. (2017)*, the basin infill is characterized by five distinct tectonostratigraphic sequences: Riachão, Jaibaras, Parnaíba, Mearim, and Grajau, separated by basin-wide unconformites. The first two sequences have been traditionally interpreted as infills resulting from Neoproterozoic (*de Castro et al., 2014*) and Cambro-Ordovician (*Oliveira and Mohriak, 2003*) rifting events, respectively, but other interpretations exist (*see Tozer et al., 2017*). The Parnaíba sequence has been attributed to cratonic subsidence, and is arranged into three megasequences also separated by regional

118 unconformities and ranging in age from Late Ordovician to Early Triassic (e.g. *Daly et al.*,
119 *2014; de Castro et al., 2014; Tozer et al., 2017*). Two magmatic events of Early Jurassic and
120 Early Cretaceous ages - expressed in the Mosquito and Sardinha formations, respectively
121 - are observed within the basin. The Mosquito Formation represents a phase of extrusive
122 volcanism related to the Central Atlantic Magmatic Province (e.g. *Góes et al., 2003*) that
123 seals the Parnaíba stratigraphy, and is overlain by the Late Jurassic Mearim sequence in the
124 center of the basin. The Sardinha Formation manifests itself as sills interfingering with basin
125 strata, and has been related to the early opening of the South Atlantic Ocean (*Merle et al.*
126 *(2011)*). The youngest sequence overlies the Parnaíba and Mearim units unconformably to
127 the North. It was deposited during Cretaceous times - likely due to processes related to the
128 opening of the South Atlantic (e.g. *Rossetti et al., 2004*) - to form the Grajau subbasin.
129 Alluvial and aeolian deposits of Cenozoic age cover large areas of the Parnaíba basin (see
130 Figure 1).

131 The Parnaíba basin is framed by the Amazonian craton to the West, the São Francisco
132 craton to the Southeast, the São Luiz craton to the North, and the Proterozoic Borborema
133 Province to the East (Fig. 1). Two of these major cratonic blocks were part of larger cra-
134 tonic landmasses (São Francisco-Congo and São Luiz-West Africa) that existed before the
135 opening of the Atlantic ocean in Mesozoic times, and likely surrounded a central Parnaíba
136 block presently concealed under the basin's sediments. The existence of a Parnaíba block
137 was postulated from geophysical evidence, petrography, and Rb-Sr and K-Ar geochronology
138 of basement rocks (*Cordani et al., 1984*), as well as from collisional tectonic models (*Brito*
139 *Neves et al., 1984; Klein et al., 2008; Nunes, 1993*), and it was regarded as one of the
140 continental fragments inherited by the South American platform after the dispersal of the
141 Rodinia supercontinent (*Fuck et al., 2008*). Analysis of recent airborne magnetic and grav-

142 ity surveys further subdivide the Parnaíba block into smaller fragments - Parnaíba North,
143 Parnaíba South, and Teresina - characterized by marked changes in magnetic properties and
144 by variations of up to 3.5 km in crustal thickness (*de Castro et al., 2014*).

145 Early geophysical studies of the Parnaíba basin, mostly based on data collected during
146 magnetic and/or gravity surveys, delineated a number of graben-like structures concealed un-
147 der the basin's sediments (e.g. *Brito Neves et al., 1984; Nunes, 1993; Cordani et al., 1984*).

148 These interpreted structures were then utilized to support models of thermo-mechanical
149 subsidence for the basin, mostly following the classical model of *McKenzie* (1978). A most
150 recent refinement of this set of models was proposed by *de Castro et al. (2014)*, from analysis
151 of airborne magnetic and gravimetric anomalies. The authors identified two sets of linear
152 trends in the basement, which were interpreted as two separate rifting stages - an older
153 one at the end of the Brasiliano orogeny and a younger one in the Cambro-Ordovician -
154 preceding major sag deposition. Interestingly, *Daly et al. (2014)* found no evidence of the
155 early Neoproterozoic phase of rifting postulated by *de Castro et al. (2014)* in their seismic
156 reflection line, and noted that the marked, subplanar unconformity imaged at the base of the
157 Phanerozoic section crossing all three crustal blocks (Borborema, Parnaíba and Amazonian)
158 might represent a major peneplanation surface. They argued that the major boundaries and
159 associated basement structures would have little to do with the formation of the basin and
160 - as the peneplain surface must postdate the complexity of the basement below - thermal
161 subsidence would become a more likely driving mechanism for the formation and evolution
162 of the Parnaíba basin.

163 The viability of the rifting model for the Parnaíba basin was extensively investigated in
164 *Tozer et al. (2017)* from modeling of Bouguer anomalies developed along the same seismic
165 transect of *Daly et al. (2014)*, backstripping of available well data, and modeling of a

166 densified seismic survey in the center of the transect. The study demonstrated - quite
167 convincingly - that a rifting model is unlikely to be able to explain the inferred crustal
168 structure and subsidence history of this basin, and postulated the existence of a 12-20 km
169 thick, lower crustal body pervading the Parnaíba block. The authors suggested that this
170 body would have resulted from magmatic intrusion of the lower crust and that it would be
171 acting as a buried load causing flexure of the basin's surface. They further argue that such
172 a model could explain, through viscoelastic stress relaxation, the long subsidence history
173 recorded in the deep wells along with the stratigraphic offlap that is well documented in at
174 the eastern edge of the basin. However, the authors caution that precise constraints on the
175 vertical emplacement of the buried load are lacking, and that geologic evidence of extensive
176 magmatism at the time of basin initiation - as expected from the large size of the postulated
177 magmatic body in the lower crust - is missing.

178 Data and data processing

179 The dataset utilized in this work was acquired by the Universidade Federal do Rio
180 Grande do Norte and the University of Cambridge as part of the broader Parnaíba Basin
181 Analysis Project (PBAP), a multi-disciplinary effort funded by BP Energy do Brasil that
182 aims at improving our current knowledge of the origin and evolution of this large cratonic
183 basin. The dataset was collected at 9 seismic stations deployed along an approximately EW
184 trending line superimposed to the seismic reflection line of *Daly et al. (2014)*. The stations
185 were interspaced at distances of 50-70 km, covering a total length of ~600 km in the central
186 portion of the basin (see Figure 1). A total of 8 seismic stations were equipped with three-
187 component, Nanometrics Meridian Compact Posthole sensors, with a frequency response flat
188 in velocity between 120 s to 108 Hz, and integrated high-gain digitizers. One station, located

189 in the center of the linear deployment, was equipped with a three-component, Güralp GMT-
190 3T sensor, also with flat response in velocity down to 120 s, and feeding a DM24 digitizer.
191 All stations operated continuously sampling at 100 samples per second and resorted to GPS
192 signal for timekeeping. The central station - contributed by the University of Cambridge -
193 was deployed in August, 2015, while the remaining broadband stations started operations
194 in March, 2016. Location coordinates and recording time windows considered for analysis
195 in this work are listed in Table 1.

196 In order to develop receiver function estimates for each of the 9 seismic stations in the
197 deployment, seismic sources with epicentral distances between 30° and 90° and magnitudes
198 above 5.5 mb were considered. Receiver functions are obtained by deconvolving the vertical
199 component of the teleseismic P-coda from the corresponding radial component, which effec-
200 tively removes the signature of the source and instrument response, and leaves the signature
201 of secondary P-to-S converted waves created at seismic discontinuities under the receiver
202 (*Langston, 1979; Ammon, 1991*). Analysis of the amplitudes and travel-times in the re-
203 ceiver functions can then be utilized to develop constraints on the seismic structure under
204 the station (*Owens et al., 1984; Ammon et al., 1990*). Moreover, the deconvolution process
205 equalizes the teleseismic waveforms, which can be stacked to produce high signal-to-noise
206 ratio estimates of the receiver response under a seismic station. The deconvolution proce-
207 dure can also be applied to the transverse component of the teleseismic P-wave coda. The
208 transverse component should be identically zero for isotropic, laterally homogenous propa-
209 gating media, so the observation of P-to-S conversions in the transverse receiver function is
210 usually diagnostic for dipping or anisotropic structures under the station (*Savage, 1998*).

211 To effectively compute receiver function estimates, the selected seismograms were cut
212 10 s before and 120 s after the P-wave arrival, demeaned, detrended, tapered with a 5%

213 cosine window, and band-pass filtered between 0.05 Hz and 4 Hz. The high-pass corner
214 frequency was selected to remove low-frequency noise from the recorded waveforms, while
215 the low-pass corner frequency was chosen to avoid aliasing before re-sampling to 10 samples
216 per second. The decimated waveforms were next rotated into the great-circle-path to obtain
217 the radial and transverse components of ground motion, and low-pass filtered with acausal
218 Gaussian filters of widths 1.0 ($f < \sim 0.5$ Hz) and 2.5 ($f < \sim 1.25$ Hz). The filtered verti-
219 cal component was then deconvolved from the corresponding filtered horizontal (radial and
220 transverse) components through the time-domain, iterative scheme of *Ligorria and Ammon*
221 (1999), with 500 iterations. The deconvolved time series were finally low-pass filtered with
222 the same Gaussian filters of widths 1.0 and 2.5 to produce low- and high-frequency receiver
223 function estimates, respectively. A strict quality control was applied to the deconvolved
224 waveforms. First, the radial receiver function was convolved back with the correspond-
225 ing vertical component to reconstruct the radial component, and those receiver functions
226 not reproducing at least 85% of the original radial component were removed. Second, the
227 transverse receiver functions were visually examined and the radial receiver functions associ-
228 ated to those exhibiting anomalously large amplitudes were excluded from further analysis.
229 Third, the remaining radial receiver functions were visually inspected for outliers, which
230 were also excluded from further analysis. A total of 165 low-frequency receiver functions
231 and 189 high-frequency receiver functions, out of 4129 waveforms selected for processing,
232 passed our quality control.

233 Average radial and transverse high-frequency receiver functions for each of the 9 stations
234 considered in this study are displayed in Figure 2. The receiver function waveforms have
235 been averaged within groups that do not exceed $\pm 5^\circ$ in back-azimuth and ± 0.05 s/km in
236 ray parameter. A close inspection of the waveforms reveals important properties about the

propagating medium. For instance, the first 3-4 s of the receiver functions are dominated by the signature of the sedimentary cover. Note that the main peak is displaced with respect to the zero lag time, which is the combined effect of a small direct P-wave followed by a large Ps conversion at the sediment-bedrock interface (see e.g. *Zelt and Ellis, 1998*). The peak and trough trailing the displaced large amplitude, at lag times around 2-3 s, are likely to be multiply reverberated phases between the surface and the sediment-bedrock interface. Luckily, the seismic energy reverberating in the sedimentary layer does not mask the signature of P-to-S conversions from deeper discontinuities. The peak at about 5 s lag time observed in most of the waveforms is consistent with a Ps conversion at the crust-mantle boundary, and the peak at about 15 s lag time is consistent with the first reverberation (PpPs phase) in the crust. The second multiple is generally harder to identify, but it can be observed at about 20 s lag time in some waveforms. The transverse components display amplitudes that are generally small when compared to the corresponding radial components, indicating that lateral variations in earth structure are small and that the medium under the stations can be regarded as laterally homogeneous. The only exception is station BDCO, for which large transverse amplitudes with opposite polarity near zero lag time suggest the presence of a strongly dipping, near-surface interface (see e.g. *Savage, 1998*).

Crustal Architecture

Crustal thickness and bulk Vp/Vs ratio

Crustal thickness and bulk Vp/Vs ratio can be estimated from receiver functions utilizing the H- κ stacking approach of *Zhu and Kanamori (2000)*. This procedure performs a grid-search over a stacking surface that is built by summing a weighted combination of Ps, PpPs

259 and PpSs+PsPs amplitudes from individual receiver functions. The Ps phase denotes a P-
 260 to-S conversion upon refraction across the Moho, while the PpPs and the PpSs+PsPs phases
 261 denotes multiple reverberations between the free surface and the Moho containing two P-
 262 wave and one S-wave segments and one P-wave and two S-wave segments, respectively (see
 263 e.g. *Ammon, 1991*). The summation is performed along the corresponding phase-moveout
 264 curves for the three phases, which are computed after assuming a simple layer-over-half
 265 space model for the receiving structure. During the calculation, the P-velocity for the layer
 266 has to be specified *a priori*, while the thickness and Vp/Vs ratio are left as free parameters.
 267 The summation of amplitudes is performed according to

$$268 \quad s(H, \kappa) = w_1 \times r(t_1) + w_2 \times r(t_2) - w_3 \times r(t_3) \quad (1)$$

269 where $r(t)$ is the radial receiver function, t_1 , t_2 and t_3 are the predicted Ps, PpPs, and
 270 PsPs+PpSs arrival times for the crustal thickness H and Vp/Vs ratio κ , and the w_i are *a*
 271 *priori* weighting factors. Crustal thickness and Vp/Vs ratios are varied within prescribed
 272 ranges, and the maximum in the $H\text{-}\kappa$ stacking surface is taken as an estimation of crustal
 273 thickness and bulk Vp/Vs ratio under the station.

274 Examples illustrating the performance of the $H\text{-}\kappa$ stacking procedure to select stations
 275 in the Parnafba basin are given in Figure 3. Note the analysis was always applied to high-
 276 frequency receiver functions to obtain the best resolution possible. The figures display the
 277 $H\text{-}\kappa$ stacking surface on top and the receiver function waveforms, sorted by ray parameter,
 278 at the bottom. In both cases a single local maximum is observed on the $H\text{-}\kappa$ stacking
 279 surface, displaying crustal thicknesses of 40.0 ± 0.4 km and 43.6 ± 0.7 km and Vp/Vs ratios
 280 of 1.70 ± 0.01 and 1.78 ± 0.03 for stations STSR and GRJU, respectively. Confidence bounds

were obtained after bootstrapping the receiver function dataset with 200 replications (*Efron and Tibshirani, 1991*). Note that, due to additional uncertainty in the assumed P-wave velocity, formal confidence bounds must be increased by ± 1 km for crustal thickness and ± 0.01 for Vp/Vs ratio (see Table 2). At station STSR, the receiver function waveforms display well-defined peaks at around 5, 16, and 20 s, which the algorithm picks as the Ps, PpPs and PpSs+PsPs phases, respectively. At station GRJU, on the other hand, the waveforms display well-defined peaks at around 5.5, 18, and 22 s for the Ps and crustal multiples, resulting in a thicker crust with larger Vp/Vs ratio.

For two of the sites, stations BPPF and GENI, we could not obtain reliable results from the H- κ stacking analysis. Lateral variations in velocity structure around these two stations might be generating inconsistent P-to-S conversions that do not stack coherently when combined all together. This was investigated by grouping the corresponding receiver functions by back-azimuth (recall Figure 2) and running the H- κ stacking separately within each group. For station BPPF, we obtained a crustal thickness of 45.8 ± 0.2 km for sources located at 166° and 42.7 ± 1.5 km for sources located at 294° , with Vp/Vs ratios of 1.73 ± 0.02 and 1.74 ± 0.03 , respectively; for station GENI, we obtained a crustal thickness of 45.1 ± 0.9 km at 293° , with a Vp/Vs ratio of 1.77 ± 0.03 . In both cases, there are back-azimuths for which the H- κ stacking did not yield any results.

A summary of crustal thicknesses and bulk Vp/Vs ratios for the broadband stations sampling the Parnaíba basin is given in Table 2. In general, we assigned weights of 0.4, 0.3, and 0.3 to the Ps, PpPs and PpSs+PsPs phases when they were clearly observed in the receiver function waveforms; however, when one of the multiples was not clearly observed, we assigned a weight of 0.0 to that phase and weights of 0.5 to the remaining phases. As no independent estimates of P-velocity exist for the basin, we opted to base our calculations on

305 the worldwide average of 6.5 km/s derived for continental crust from crustal compilations
306 (*Christensen and Mooney, 1995*) and assess variations in the inferred crustal values for P-
307 velocities varying between 6.3 and 6.7 km/s. The results in Table 2 reveal that crustal
308 thicknesses range between 39 and 46 km and have combined confidence bounds of ± 2 km, if
309 we assume uncertainties in P-velocity of ± 0.1 km/s. Vp/Vs ratios are more variable and less
310 well-constrained, although most of the measurements range between 1.69 and 1.76 and have
311 combined confidence bounds below ± 0.08 . Note that, for Vp/Vs ratios, uncertainties due
312 to variation in P-velocity are significantly smaller than those obtained from bootstrapping
313 the dataset. The resulting variation in crustal thickness along the deployment is further
314 illustrated in Figure 4. The figure reveals the crust thickens from 40-42 km at the edges to
315 43-46 km near the depocenter (stations GRJU, GENI and BDCO), and that this thickening
316 is accompanied by an increase in Vp/Vs ratio from 1.70-1.72 at the edges to 1.77-1.78 near
317 the depocenter. This trend in Vp/Vs is somehow disrupted by station PRDT, but the
318 confidence bounds are large and can be accommodated.

319 S-wave velocity-depth profiles

320 S-wave velocity-depth profiles for each individual station along the transect were devel-
321 oped by inverting the receiver function waveforms in this study jointly with independent
322 surface-wave dispersion velocities. We followed the approach of *Julia et al. (2000; 2003)*, in
323 which a linear combination of the root-mean-square error for both datasets and a roughness
324 norm for the velocity model are minimized through a linearized, iterative inversion scheme.
325 In that approach, the datasets are equalized for the different number of data points and
326 physical units through normalization by $N\sigma^2$, where N is the number of data points and σ^2
327 is the data variance, and pre-multiplied by an influence factor ($0 < p < 1$) that controls

328 the relative contribution of each data set to the total norm. Following previous studies (e.g.
329 *Julia et al., 2003; 2008*), we considered an influence factor of 0.5 - giving equal importance
330 to each data set - and average variances of 0.0001 s^{-2} and 0.0025 (km/s)^2 for the receiver
331 functions and dispersion velocities, respectively. In general, 6 iterations sufficed to achieve
332 convergence.

333 The starting model adopted during the inversion consisted of a perfectly elastic, laterally
334 homogeneous and isotropic medium defined through a stack of thin layers of fixed thickness
335 and uniform velocity. The crust has a linear velocity increase from 3.4 km/s at the surface
336 to 4.0 km/s at 42.5 km depth and overlies a 4.5 km/s upper mantle. The top two layers are
337 1.0-2.0 km thick, with thicknesses carefully chosen for each station to precisely match P-to-
338 S amplitudes from the sediment-bedrock interface in the first 3-4 s of the receiver function
339 waveforms. This forward modeling exercise was important, as we observed uppermost crustal
340 velocities may trade-off with sedimentary structure. Layer thicknesses then progressively
341 increase from 2.5 km at crustal levels to 5 km in the lithospheric mantle and to 10 km down
342 to 220 km depth, thus reflecting the decrease in resolution with depth associated to the
343 datasets (see e.g. *Julia et al., 2003*). As dispersion velocities have partial sensitivity to
344 deep mantle structure at long periods, the starting model is further parameterized down to
345 ~500 km depth with flattened PREM velocities (*Dziewonski and Anderson, 1981*), which
346 are constrained to remain unchanged during successive iterations. A flattened PREM might
347 not be the actual structure in the deep mantle under the Parnaíba basin, but will suffice to
348 account for the partial sensitivity of dispersion velocities (see *Julia et al., 2003*).

349 Dispersion velocities were borrowed from the continental-scale, surface-wave tomography
350 study of *Feng et al. (2004)*. In that study, local group-velocity dispersion curves for the
351 fundamental-mode of Rayleigh-waves were developed for periods between 10 and 140 s for the

352 South American continent. Single-station measurements at broadband stations widespread
353 throughout the continent were first taken on the vertical component of regional seismograms
354 collected between 1990 and 2003, with sources located mainly along plate boundaries. This
355 resulted in over 6,000 single-station dispersion curves that were then tomographically in-
356 verted to develop local dispersion curves within cells that formed a $1^{\circ} \times 1^{\circ}$ grid covering the
357 entire continent. Although not reported in the study, uncertainties were estimated to range
358 from ± 0.05 km/s at short periods to ± 0.12 km/s at longer periods (M. Assumpção, pers.
359 comm., 2008). The velocity-depth profiles presented in our study were thus developed by
360 jointly inverting the receiver functions at a given station with the local dispersion curve
361 associated to the tomographic cell enclosing that station.

362 The performance of the joint inversion procedure is illustrated in Figure 5 through sta-
363 tions STSR and GRJU, which are located on opposite sides of the transect. The figure
364 displays the starting and final joint inversion models, along with the fits between observed
365 and predicted receiver functions and Rayleigh-wave dispersion curves for each station. Note
366 that the receiver function dataset includes all the averages at high- and low-frequency con-
367 tents developed for a given station (recall Figure 2). The match between observations and
368 predictions is excellent in both cases, with the fine layering introduced at the top of the
369 model successfully accounting for observed variations in receiver function amplitudes during
370 the first 3-4 seconds in the waveforms. For station STSR, the inverted velocity-depth profiles
371 is simple, and reveals a ~ 38.0 km thick crust with a smooth velocity increase with depth,
372 an upper crust of ~ 3.5 km/s down to ~ 18 km depth, and a lower crust varying between
373 3.6 and 3.9 km/s down to Moho depths; for station GRJU, the crust is 41-43 km thick and
374 displays a 3.5-3.6 km/s upper crust down to ~ 19 km depth overlying a 3.7-3.8 km/s lower
375 crust down to Moho depths. Sediment thicknesses are 2.0 km for station STSR and 3.5 km

376 for station GRJU. The crust-mantle boundary is modeled as a sharp discontinuity under
377 station STSR, and as a gradational transition under station GRJU, as expected from the
378 comparatively small amplitudes displayed by the crustal multiples in comparison to the Ps
379 phase (e.g. *Julia, 2007*). Upper mantle velocities are around 4.5-4.6 km/s for both stations.

380 Confidence bounds for the S-velocity model at a given station were developed after
381 jointly inverting high- and low-frequency receiver functions within each group with the
382 dispersion curve for that seismic station. This resulted in the development of several velocity
383 models for each station (i.e. 4 at station STSR and 5 at station GRJU), which were then
384 utilized to compute the standard deviation in S-velocity for each layer with respect to the
385 "average" velocity model (i.e. the model from the joint inversion of all receiver function
386 groups and the dispersion curve). Confidence bounds were reported as grey bands around
387 the "average" velocity model, marking the 2σ -variation in S-velocity for each layer. Figure 5
388 shows that confidence bounds are ± 0.1 km/s down to 80-90 km depth and may grow to ± 0.2
389 km/s at larger depths, although they may locally grow bigger if lateral variations in earth
390 structure around the station are required to match features unique to a particular receiver
391 function group. Given the parameterization of our models, uncertainties in the depth of the
392 discontinuities are at least one layer thickness, this is, ± 2.5 km.

393 A summary of the S-velocity models developed for the stations in the Parnaíba basin is
394 displayed in Figure 6. Within confidence bounds, the velocity-depth profiles corroborate the
395 results from the H- κ stacking analysis and reveal a thickening of the crust around station
396 GENI, near the basin's depocenter. The profiles also show the crust is generally structured
397 in two layers: (i) a 15-20 km thick upper crust with S-velocities around 3.5-3.6 km/s, and (ii)
398 a 18-22 km thick lower crust with S-velocities around 3.7-3.8 km/s. However, under station
399 GENI - where the crust is thickest - the bottom 10-12 km of the crust are characterized by

400 faster velocities of 4.0-4.2 km/s. Such a high-velocity lower crust is not observed under the
401 other stations. In the upper mantle, velocities are 4.5-4.6 km/s immediately below the Moho
402 and slowly increase to faster values with depth. The sediment-bedrock interface is located
403 at 1.5-3.5 km depth, thickening towards the depocenter, and sediments display velocities in
404 the 1.7-2.4 km/s range. The figure also superimposes the depths of the main crustal features
405 outlined in the crustal model of *Tozer et al.* (2017) from analysis of seismic reflection and
406 gravity data. Crustal thicknesses are generally similar, but the receiver function models
407 require a thickening under stations GRJU, GENI, and BDCO, and a slight thinning under
408 stations STSR and BUCO, that does not seem to be required in their model. Similarly, an
409 upper-lower crust interface is observed in both the gravity and receiver function models at
410 similar depth ranges, but the respective topographies do not precisely match. The agreement
411 for the sediment-bedrock interface is remarkable, considering the simple forward-modeling
412 approach utilized in the receiver function modeling.

413 Implications for basin subsidence

414 The results on crustal thickness and velocities reported in the previous section have re-
415 vealed that the crust thickens from 39-42 km at the edges to 43-45 km near the depocenter,
416 and that the thickening is accompanied by: (i) an increase in Vp/Vs ratio from 1.70-1.75 to
417 1.77-1.78, and (ii) by a layer of fast-velocity material of 4.0-4.2 km/s at the bottom of the
418 crust. Our crustal thicknesses are thus at odds with models of basin evolution that invoke
419 initial mechanical stretching of the basin's lithosphere. According to global compilations
420 (e.g. *Durrheim and Mooney, 1991; Zandt and Ammon, 1995*), the crust of Precambrian
421 terrains worldwide is between 35 and 45 km thick. A crustal thickness range of 39-45 km for
422 the Parnaíba block can therefore be regarded as average. Moreover, an average crustal thick-

ness indicates that if mechanical stretching occurred before subsidence, the corresponding stretching factor was small. Small stretching factors imply minimal subsidence from initial mechanical stretching and from subsequent cooling of the advected asthenosphere (*McKenzie, 1978*). Thus, a crustal thickness range of 39-45 km, consistent with crustal thickness of outcropping Precambrian terrains worldwide, indicates that mechanical stretching of the Parnaíba basin - if it existed at all - did not play a significant role during its formation and further evolution.

Our results do not support either a pervasive body of magmatic intrusives making the lower crust of the Parnaíba block, as suggested in *Tozer et al. (2017)*. Laboratory measurements in rock samples show that typical Vp/Vs ratios for mafic lower crustal lithologies - i.e. mafic granulite and mafic garnet granulite - are around 1.81 - 1.82 (*Christensen, 1996*), so a mafic lower crust should increase the bulk Vp/Vs ratio for the entire crustal column. Back-of-the-envelope calculations show that a bulk Vp/Vs ratio of 1.76 is compatible with the presence of a layer of 5-6 km of mafic material in the lower crust (see *Luz et al., 2015*); a thicker layer, however, should increase the bulk Vp/Vs ratio above 1.76. Our bulk Vp/Vs ratios range between 1.70 and 1.75 along the edges of the profile, and grow to 1.77-1.78 near the depocenter, which suggests that magmatic intrusives are restricted to the region where the crust is thickest. Moreover, using a P-velocity range of 7.0 - 7.6 km/s for mafic lower crustal material (*Durrhem and Mooney, 1991*) and the Vp/Vs ratios of *Christensen (1996)*, we conclude that S-velocities in the 3.9 - 4.2 km/s range may correspond to mafic rocks. Only the fast velocity layer in the bottom 10-12 km under station GENI falls within that velocity range, further confirming our suspicion that magmatic intrusives do not pervade the lower crust.

The lack of a pervasive mafic lower crust under the Parnaíba basin may have implications

for understanding the depositional history of this basin. As outlined in Section 2, *Tozer et al. (2017)* have recently proposed that cratonic subsidence of the Parnaíba basin might be due to flexural bending driven by a buried load, and identified a postulated mafic lower crust for the Parnaíba block - along with sediment weight - as such buried load. The lack of a pervasive, high-density lower crustal body - as suggested by our S-velocity models - considerably reduces the load available for driving subsidence, and limits its ability to induce viscoelastic stress relaxation of the lithosphere (required to explain the long subsidence history of this basin). Alternatively, our smaller mafic body might be linked to a heating event ultimately responsible for basin subsidence. Indeed, *Daly et al. (2014)* found their results on the reflectivity structure of the Parnaíba basin to be consistent with thermal subsidence. However, we noticed that the large Vp/Vs ratios and the fast-velocity body in the lower crust coincide pretty closely with the location of the thickest cumulative isopachs for the Early Cretaceous Sardinha formation (see Figure 7), which makes us think that the fast lower-crustal body might have a similar origin. If our conclusion is correct, that would imply that the emplacement of the mafic body in the depocenter postdated the initiation of cratonic subsidence and invalidate the mafic layer as a valid remnant of the postulated heating event.

Convection processes in the deep mantle, on the other hand, have been shown to be capable of triggering vertical movements in the overlying lithosphere, and have been invoked to explain - for instance - the elevated topography of the South African Plateau (e.g. *Lithgow-Berteloni and Silver, 1998; Gurnis et al., 2000*). Similarly, cold-spots associated with convective downwellings may be capable of explaining the origin of regional subsidence (*Hartley and Allen, 1994*). Such downwellings have been invoked to explain the subsidence mechanism, for instance, of the Congo basin in Africa (*Downey et al., 2011*); after an initial

⁴⁷¹ stage of uplift caused by isostatic rebound following delamination, a vertical downwelling
⁴⁷² would have been caused by the sinking of the delaminated lithospheric fragment, which
⁴⁷³ would in turn drag the overlying lithosphere and cause subsidence of the initially elevated
⁴⁷⁴ region. *Tozer et al.* (2017) caution that precise constraints on the vertical emplacement
⁴⁷⁵ of the buried load are lacking, opening the possibility of such buried load to be emplaced
⁴⁷⁶ deeper in the mantle. Determination of lithospheric thickness, as well as imaging of the
⁴⁷⁷ sublithospheric mantle, is thus required to assess the plausibility of such mechanisms for the
⁴⁷⁸ Parnaíba basin.

⁴⁷⁹ Conclusions

⁴⁸⁰ We have developed 9 point estimates of crustal thickness and bulk Vp/Vs ratio across
⁴⁸¹ the Parnaíba basin of NE Brazil, along with detailed velocity-depth profiles of S-velocity.
⁴⁸² Our results are consistent with the presence of a mafic layer in the lower crust near the
⁴⁸³ depocenter of the basin, which is characterized by a thickness of 10-12 km and crustal S-
⁴⁸⁴ velocities varying between 4.0 and 4.2 km/s. The crustal architecture of the block is similar
⁴⁸⁵ to that of Precambrian terrains worldwide, suggesting minimal stretching of the basin's
⁴⁸⁶ underlying basement. Elastic flexure by a deep load is favored as a mechanism for the origin
⁴⁸⁷ and evolution of cratonic subsidence in the basin. However, such load cannot be attributed
⁴⁸⁸ to a pervasive intrusive body in the lower crust and propose deep mantle loads, perhaps
⁴⁸⁹ related to convective processes, as a more plausible candidates. Deep mantle structure,
⁴⁹⁰ nonetheless, needs to be investigated in order to assess the role of such deep convective
⁴⁹¹ processes in the formation and evolution of this cratonic basin.

⁴⁹² Acknowledgements

493 We thank an anonymous reviewer and the Associate Editor handling the submission, Dr.
494 Anthony Watts, for carefully reading the original manuscript and for constructive criticism
495 that significantly improved the discussion and presentation of our results. Acquisition and
496 analysis of the dataset presented in this study was funded through a grant awarded by BP
497 Energy do Brasil. Diogo L.O.C. additionally thanks BP Energy do Brasil for a generous
498 scholarship to complete his PhD degree at the Universidade Federal do Rio Grande do Norte.
499 Jordi Julià also thanks BP Energy do Brasil for awarding a research fellowship to conduct
500 this research.

501 References

- 502 Almeida, F.F.M., Hasui, Y., Brito Neves, B.B., Fuck, R.A. (1981). Brazilian structural
503 provinces: An introduction, *Earth Sci. Rev.*, **17**, 1-29.
- 504 Ammon, C.J. (1991). The isolation of receiver effects from teleseismic P waveforms,
505 *Bull. Seism. Soc. Am.*, **81**, 2504-2510.
- 506 Ammon, C. J., Randall, G.E., Zandt, G. (1990). On the non-uniqueness of receiver
507 function inversions, *J. Geophys. Res.*, **95**, 15,303-15,318.
- 508 Assumpção, M., Feng, M., Tassara, A., Julià, J. (2013a). Models of crustal thickness
509 for South America from seismic refraction, receiver functions and surface wave tomography,
510 *Tectonophysics*, **609**, 82-96.
- 511 Assumpção, M., Bianchi, M., Julià, J., Dias, F.L., França, G.S., Nascimento, R.M.N.,
512 Drouet, S., Pavão, C.S., Albuquerque, D.F., Lopes A.E.V. (2013b), Crustal thickness map
513 of Brazil: Data compilation and main features, *J. South Am. Earth Sci.*, **43**, 74-85.
- 514 Brito Neves, B.B., Fuck, R.A., Cordani, U.G., Thomas, A. (1984). Influence of basement
515 structures on the evolution of the major sedimentary basins of Brazil: A case of tectonic
516 heritage, *J. Geodyn.*, **1**, 495-510.
- 517 Brito Neves, B.B., Fuck, R.A. (2013). Neoproterozoic evolution of the basement of the
518 South American Platform, *J. South Am. Earth Sci.*, **47**, 72-89.
- 519 Cloetingh, S., Burov, E. (2011). Lithospheric folding and sedimentary basin evolution:
520 a review and analysis of formation mechanisms, *Basin Res.*, **23**, 257-290.
- 521 Christensen, N. I. (1996). Poissons ratio and crustal seismology, *J. Geophys. Res.*, **101**,
522 3139-3156.

- 523 Christensen, N.I., Mooney, W.D. (1995). Seismic velocity structure and composition of
524 the continental crust: A global view, *J. Geophys. Res.*, **100**, 9761-9788.
- 525 Cordani, U.G., Brito Neves, B.B., Fuck, R.A., Porto, R., Thomaz Filho, A., Cunha,
526 F.M.B. (1984). Estudo preliminar de integração do Pré-Cambriano com os eventos tectônicos
527 das bacias sedimentares brasileiras, *Ciência Técnica Petróleo, Seção Exploração de Petróleo*,
528 Rio de Janeiro 15, p70.
- 529 Cordani, U.G., Brito Neves, B.B., Thomaz Filho, A. (2009). Estudo preliminar de
530 integração do Pré-Cambriano com os eventos tectônicos das bacias sedimentares brasileiras
531 (Atualização), *Bol. Geociênc. Petrobras*, Rio de Janeiro **17** (1), 205-219.
- 532 Cordani, U.G., Pimentel, M.M., Araujo, C.E.G., Fuck, R.A. (2013). The significance of
533 the Transbrasiliano-Kandi tectonic corridor for the amalgamation of West Gondwana, *Braz.
534 J. Geol.*, **43**, 583-597.
- 535 Daly, M.C., Andrade, V., Barousse, C.A., Costa, R., McDowell, K., Piggot, N., Poole,
536 A.J. (2014). Brasiliano crustal structure and the tectonic setting of the Parnaíba basin of NE
537 Brazil: Results of a deep seismic reflection profile, *Tectonics*, **33**, doi:10.1002/2014TC003632.
- 538 de Castro, D.L., Fuck, R.A., Phillips, J.D., Vidotti, R.M., Bezerra, F.H.R., Dantas, E.L.
539 (2014). Crustal structure beneath the Paleozoic Parnaíba Basin revealed by airborne gravity
540 and magnetic data, Brazil, *Tectonophysics*, **614**, 128-145.
- 541 Downey, N., Gurnis, M., Avouac, J.-P. (2011). Subsidence history and geodynamic
542 evolution of the cratonic Congo Basin, *Geophys. Res. Abstracts*, **13**, EGU2011-388-1.
- 543 Durrheim, R. J., Mooney, W.D. (1991). Archean and Proterozoic crustal evolution:
544 Evidence from crustal seismology, *Geology*, **19**, 606-609.

- 545 Dziewonsky, A.M., Anderson, D.L. (1981). Preliminary reference earth model, *Phys.*
546 *Earth Planet. Int.*, **25**, 297-356.
- 547 Efron, B., Tibshirani, R. (1991). Statistical data analysis in the computer age, *Science*,
548 **253**, 390-395.
- 549 Feng, M., Assumpção, M., van der Lee, S. (2004). Group-velocity tomography and
550 lithospheric S-velocity structure of the South American continent, *Phys. Earth Planet.*
551 *Inter.*, **147**, 315-331.
- 552 Feng, M., Van der Lee, S., Assumpção (2007). Upper mantle structure of South America
553 from joint inversion of waveforms and fundamental-mode group velocities of Rayleigh waves,
554 *J. Geophys. Res.*, **112**, B04312, doi:10.1029/2006JB004449.
- 555 Fuck, R.A., Brito Neves, B.B., Schobbenhaus, C. (2008). Rodinia descendants in South
556 America, *Precambrian Res.*, **160**, 108-126.
- 557 Gilbert, A., Sheehan, A.F. (2004). Images of crustal variations in the intermountain
558 west, *J. Geophys. Res.*, **109**, 1978-2012.
- 559 Góes, A.M.O., Feijó, F.J. (1994), Bacia do Parnaíba, *Boletim de Geociências da Petro-*
560 *bras*, **8**, 57-67.
- 561 Góes, A.M.O., Travassos, W.A.S., Nunes, K.C. (1993). Projeto Parnaíba: Reavaliação
562 e perspectivas exploratórias, paper presented at Relatório Petrobras, DEXNOR-DINTER.
- 563 Gurnis, M., Mitrovica, J.X., Ritsema, J., van Heijst, H.J. (2000). Constraining mantle
564 density structure using geological evidence of surface uplift rates: The case of the African
565 Superplume, *Geochem. Geophys. Geosyst.*, **1**, 1999GC000035.
- 566 Hartley, R.W., Allen, P.A. (1994). Interior cratonic basins of Africa: Relation to conti-

- 567 nental break-up and role of mantle convection, *Basin Res.*, **6**, 95-113.
- 568 Julià, J., Ammon, C.J., Herrmann, R.B., Correig, A.M. (2000). Joint inversion of re-
569 ceiver functions and surface-wave dispersion ob- servations, *Geophys. J. Int.*, **143**, 99-112.
- 570 Julià, J., Ammon, C.J., Herrmann, R.B. (2003). Lithospheric structure of the Ara-
571 bian Shield from the joint inversion of receiver functions and surface-wave group velocities,
572 *Tectonophysics*, **371**, 1-21.
- 573 Julià, J. (2007). Constraining velocity and density contrasts across the crust mantle
574 boundary with receiver function amplitudes, *Geophys. J. Int.*, **171**, 286-301.
- 575 Julià, J., Assumpção, M., Rocha, M.P. (2008), Deep crustal structure of the Paraná
576 Basin from receiver functions and Rayleigh-wave dispersion: Evidence for a fragmented
577 cratonic root, *J. Geophys. Res.*, **113**, B08318, doi:10.1029/2007JB005374.
- 578 Kaminski, E., Jaupart, C. (2000). Lithosphere structure beneath the Phanerozoic in-
579 tracratonic basins of North America, *Earth Planet. Sci. Lett.*, **178**, 139-149.
- 580 Klein, G. deV., A.T. Hsui (1987) Origin of cratonic basins, *Geology*, **15**, 1094-1098.
- 581 Klein, E.L., Luzardo, R., Moura, C.A.V., Armstrong, R. (2008). Geochemistry and
582 zircon geochronology of Paleoproterozoic granitoids: further evidence on the magmatic and
583 crustal evolution of the São Luís cratonic fragment, Brazil, *Precambrian Res.*, **165**, 221-242.
- 584 Langston, C.A. (1979). Structure under Mount Rainier, Washington, inferred from tele-
585 seismic body waves, *J. Geophys. Res.*, **84**, 4749-4762.
- 586 Ligorría, J.P., Ammon, C.J. (1999). Iterative deconvolution and receiver function esti-
587 mation, *Bull. Seism. Soc. Am.*, **89**, 1395-1400.
- 588 Lithgow-Bertelloni, C., Silver, P.G. (1998), Dynamic topography, plate driving forces,

589 and the African superswell, *Nature*, **395**, 269-273.

590 Lloyd, S., van Der Lee, S., França, G.S., Assumpção, M., Feng, M. (2010). Moho map of

591 South America from receiver functions and surface waves, *J. Geophys. Res.*, **115**, B11315,

592 doi:10.1029/2009JB006829.

593 Luz, R.M.N., Julià, J., do Nascimento, A.F. (2015). Bulk crustal properties of the

594 Borborema Province, NE Brazil, from P-wave receiver functions: Implications for models of

595 intraplate Cenozoic uplift, *Tectonophysics*, **644-645**, 81-91.

596 McKenzie, D. (1978), Some remarks on the development of sedimentary basins, *Earth*

597 *Planet. Sci. Lett.*, **40**, 25-32.

598 Merle, R., Marzoli, A., Bertrand, H., Reisberg, L., Verati, C., Zimmermann, C., Chiara-

599 dia, M., Bellieni, G., Ernesto, M. (2011). $^{40}\text{Ar}/^{39}\text{Ar}$ ages and Sr-Nd-Pb-Os geochem-

600 istry of CAMP tholeiites from western Maranhão basin (NE Brazil), *Lithos*, **122**, 137-151,

601 doi:10.1016/j.lithos2010.12.010.

602 Nunes, K.C. (1993). Interpretação integrada da Bacia do Parnaíba com ênfase nos dados

603 aeromagnéticos, 3rd International Congress of the Brazilian Geophysical Society, Expanded

604 Abstracts, pp. 152-157.

605 Oliveira, D. C., Mohriak, W.U., (2003), Jaibaras Trough: An important element in the

606 early tectonic evolution of the Parnaíba interior sag basin, Northern Brazil, *Mar. Pet. Geol.*,

607 **20**, 351-383.

608 Owens, T.J., Zandt, G., Taylor, S.R. (1984). Seismic evidence for an ancient rift be-

609 neath the Cumberland Plateau, Tennessee: a detailed analysis of broadband teleseismic P

610 waveforms, *J. geophys. Res.*, **89**, 7783-7795.

- 611 Rossetti, D.F., Paz, J.D.S., Góes, A.M.O. (2004). Facies analysis of the Codó formation
612 (late Aptian) in the Grajaú area, southern São Luís-Grajaú Basin, An. Acad. Bras. Cienc.,
613 76, 791-806, doi:10.1590/S0001-37652004000400012.
- 614 Schimmel, M., Paulssen, H. (1997). Noise reduction and detection of weak, coherent
615 signals through phase-weighted stacks. *Geophys. J. Int.*, **130**, 497-505.
- 616 Tozer, B., Watts, A.B., Daly, M.C. (2017). Crustal structure, gravity anomalies, and
617 subsidence history of the Parnaíba cratonic basin, Northeast Brazil. *J. Geophys. Res.*, **122**,
618 doi:10.1002/2017JB014348.
- 619 Uieda, F., Barbosa V.L.F. (2017). Fast nonlinear gravity inversion in spherical coordi-
620 nates with application to the South American Moho, *Geophys. J. Int.*, **208**, 162-176.
- 621 van der Meijde, M., Julià, J., Assumpção, M. (2013). Gravity derived Moho for South
622 America, *Tectonophysics*, **609**, 456-467.
- 623 Vaz, P.T., Rezende, N.A.M., Filho J.R.W., Travassos, W.A.S. (2007). Bacia do Parnaíba,
624 *Boletim de Geociências da Petrobrás*, textbf{2}, 253-263.
- 625 Zandt, G., Ammon, C.J. (1995). Continental crust composition constrained by measure-
626 ments of crustal Poisson's ratio, *Nature*, **374**, 152-154.
- 627 Zelt, B.C., Ellis, R.M. (1998). Receiver function studies in the Trans-Hudson orogen,
628 Saskatchewan, *Can. J. Earth Sci.*, **36**, 585-603.
- 629 Zhu, L., Kanamori, H. (2000). Moho depth variation in southern California from tele-
630 seismic receiver functions, *J. Geophys. Res.*, **105**, 2962-2980.

₆₃₁ **Tables**

Table 1: *Station coordinates and recording time windows for stations in the Parnaíba basin.*

Station	Latitude (deg)	Longitude (deg)	Recording time (YYYY.JJJ)*
BPPF	-6.2271	-47.2518	2016.188 – 2017.199
BUCO	-5.1586	-43.2010	2016.118 – 2017.199
GENI	-5.4612	-45.5344	2016.105 – 2017.199
GRJU	-5.8308	-46.0882	2016.104 – 2017.199
PRDT	-5.3241	-44.3974	2016.106 – 2017.200
STSN	-6.0787	-46.5986	2016.105 – 2017.199
STSР	-5.2889	-43.8063	2016.119 – 2017.199
TRZN	-5.1056	-42.6344	2016.118 – 2017.199
BDCO	-5.4517	-45.0203	2015.222 – 2016.293

* Recording time window is given as year (YYYY) and Julian day (JJJ).

Table 2: $H\text{-}\kappa$ stacking parameters for varying values of V_p .

Station	n	w1,w2,w3	$H \pm 2\sigma$ (km)					Vp/Vs $\pm 2\sigma$		
			Vp 6.3	Vp 6.4	Vp 6.5	Vp 6.6	Vp 6.7	Vp 6.3	Vp 6.4	Vp 6.5
BDCO	17	0.4,0.3,0.3	41.9 \pm 0.5	42.7 \pm 0.5	43.7 \pm 0.5	44.5 \pm 0.5	45.5 \pm 0.6	1.74 \pm 0.02	1.73 \pm 0.02	1.73 \pm 0.02
BPPF [†]	2	0.5,0.5,0.0	44.1 \pm 0.2	45.0 \pm 0.2	45.8 \pm 0.2	46.7 \pm 0.2	47.2 \pm 0.2	1.74 \pm 0.02	1.74 \pm 0.02	1.73 \pm 0.02
	4	41.1 \pm 1.3	41.9 \pm 1.5	42.7 \pm 1.5	43.6 \pm 1.4	44.4 \pm 1.5	45.5 \pm 1.5	1.75 \pm 0.03	1.75 \pm 0.03	1.74 \pm 0.03
BUCO	21	0.4,0.3,0.3	37.8 \pm 0.5	38.5 \pm 0.6	39.3 \pm 0.5	40.1 \pm 0.4	40.9 \pm 0.6	1.75 \pm 0.02	1.74 \pm 0.02	1.73 \pm 0.02
	4	0.5,0.5,0.0	42.1 \pm 0.7	43.4 \pm 0.8	45.1 \pm 0.8	45.9 \pm 0.9	46.8 \pm 0.9	1.78 \pm 0.03	1.78 \pm 0.03	1.77 \pm 0.03
GENT*	28	0.4,0.3,0.3	42.1 \pm 0.7	42.9 \pm 0.7	43.6 \pm 0.7	44.5 \pm 0.7	45.3 \pm 0.7	1.78 \pm 0.02	1.78 \pm 0.03	1.78 \pm 0.02
	19	0.4,0.3,0.3	39.5 \pm 1.5	40.2 \pm 2.1	41.1 \pm 1.9	42.0 \pm 2.0	42.8 \pm 1.8	1.78 \pm 0.06	1.78 \pm 0.06	1.77 \pm 0.07
PRDT	24	0.4,0.3,0.3	40.5 \pm 0.8	41.3 \pm 0.9	42.2 \pm 0.7	43.1 \pm 0.7	43.9 \pm 1.0	1.75 \pm 0.02	1.73 \pm 0.02	1.73 \pm 0.02
	20	0.4,0.3,0.3	38.4 \pm 0.4	39.2 \pm 0.4	40.0 \pm 0.4	40.7 \pm 0.4	41.5 \pm 0.5	1.71 \pm 0.01	1.71 \pm 0.01	1.70 \pm 0.01
TRZN	22	0.4,0.3,0.3	38.7 \pm 1.1	39.5 \pm 0.9	40.3 \pm 1.1	41.0 \pm 0.7	41.8 \pm 1.3	1.73 \pm 0.03	1.72 \pm 0.03	1.71 \pm 0.03

The table includes the number of waveforms (n), P-wave velocity assumed (Vp) in km/s, and weights for the Ps (w1), PpPs (w2), and PpSs + PsPs (w3) phases, respectively.

* Results for station GENI are restricted to events approaching the station at $\sim 293^\circ$ back-azimuth.

[†] Results for station BPPF are restricted to events approaching the station at $\sim 166^\circ$ (top) and $\sim 294^\circ$ (bottom) back-azimuth.

632 Figure Captions

633 **Figure 1** - Geological map of the Parnaíba basin displaying the location of Parnaíba
634 Basin Analysis Project (PBAP) stations (triangles) utilized in this study. AM - Amazonian
635 Craton; BB - Borborema Province; SF - São Francisco Craton; SL - São Luís Craton; TO -
636 Tocantins Province.

637 **Figure 2** - Receiver function stacks developed for the seismic stations in the Parnaíba
638 basin. Top and bottom traces refer to radial and transversal receiver functions, respectively.
639 The number of waveforms included in the stack, average back-azimuth, and average ray
640 parameter are displayed in the upper right corner of each panel. The stacks are presented
641 through a black line within a gray shade representing 1σ -confidence bounds for the stacked
642 amplitudes.

643 **Figure 3** - Sample H- κ stacking results for station STSR and GRJU. The top panels
644 display the H κ stacking surfaces, while the bottom panels display the corresponding radial
645 receiver functions utilized during the stacking procedure, sorted by ray parameter. The
646 thick, red line in the top panels is the 1σ -confidence ellipse from bootstrapping, and the
647 thin, red lines in the bottom panels are the phase moveout curves for the Ps, PpPs and
648 PpSs+PsPs phases associated to the maximum in the H κ -stacking surface.

649 **Figure 4** - H- κ stacking results for Vp/Vs ratio (top) and crustal thickness (bottom)
650 for all the stations in the Parnaíba basin. The vertical lines represent 2σ confidence bounds,
651 while the red stripes mark the regions of 1.70-1.72 and 40-42 km variation in Vp/Vs ratio
652 and crustal thickness, respectively. Note the thickening and increase in Vp/Vs ratio around
653 stations GRJU, GENI, and BDCO.

654 **Figure 5** - Joint inversion results for stations GRJU (left) and STSR (right). Com-

parison between observed (black) and predicted (red) receiver functions are shown in the upper-left panels, while comparison between observed (black triangles) and predicted (red line) group velocities are shown in the lower-left panels. The inverted (black line) and initial (blue line) S-velocity models are displayed in the right panels, along with the 2σ -confidence bounds for the inverted velocities (grey band). The numbers next to the receiver function waveforms indicate the number of waveforms (n), the average back-azimuth (baz) and standard deviation (sdbaz), and the average ray parameter (rayp) and standard deviation (sdrayp), according to (n) $\text{baz}|p_{\text{msdbaz}}$ $\text{rayp} \pm \text{sdrayp}$.

Figure 6 - Joint inversion S-velocity models for each station along the profile, sorted according to station location. Inverted models are shown as black lines, with grey bands marking the 2σ -confidence bounds. H- κ stacking results for crustal thickness are superimposed as red, transparent bands, for comparison. The main layer boundaries for the sediment-bedrock interface (purple), the upper-lower crust interface (blue) and crust-mangle boundary (green) from the seismic and gravity model of *Tozer et al. (2017)* have been superimposed to the velocity models. Note the thicker crust under stations GRJU, GENI, and BDCO, predicted by the joint inversion models.

Figure 7 - Cumulative isopach map for the Sardinha Formation with the location of our seismic stations superimposed. The Figure also displays the location of the seismic reflection line of *Daly et al. (2014)*, along with the location of the Mid Crustal Reflector (MCR) imaged in their study. Note how stations GRJU, GENI, and BDCO are located on top of the thickest magmatic accumulation.

676 **Figures**

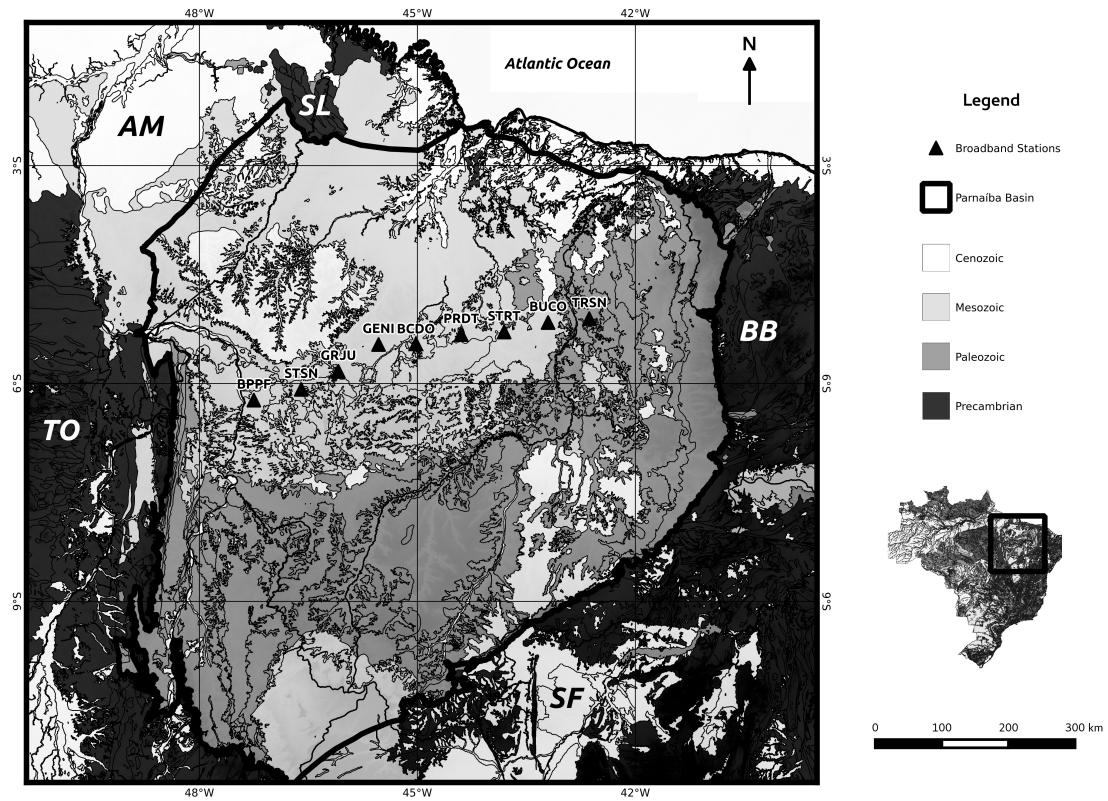


Figure 1: Geological map of the Parnaíba basin displaying the location of Parnaíba Basin Analysis Project (PBAP) stations (triangles) utilized in this study. AM - Amazonian Craton; BB - Borborema Province; SF - São Francisco Craton; SL - São Luís Craton; TO - Tocantins Province.

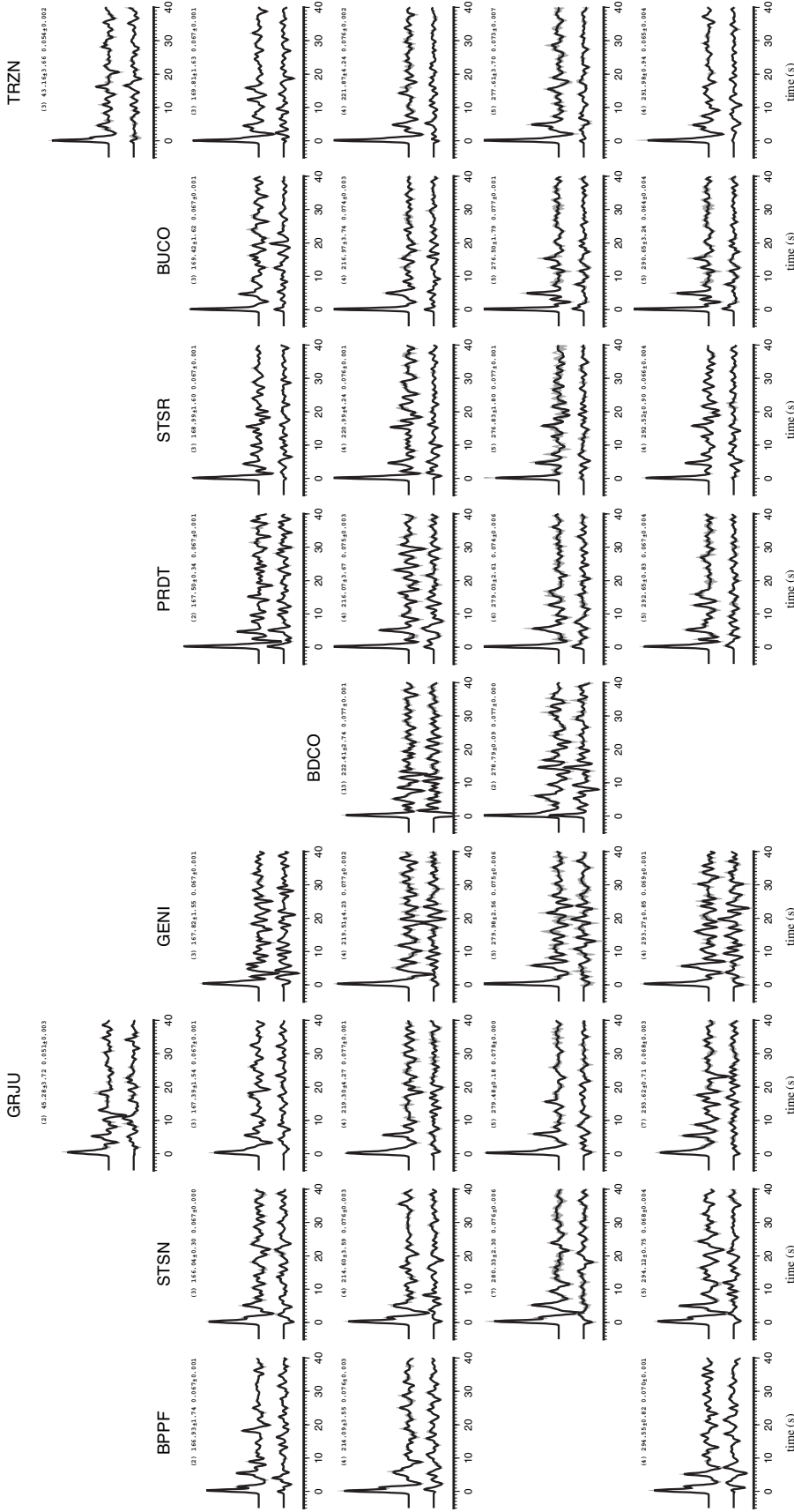


Figure 2: Receiver function stacks developed for the seismic stations in the Paranaíba basin. Top and bottom traces refer to radial and transversal receiver functions, respectively. The number of waveforms included in the stack, average back-azimuth, and average ray parameter are displayed in the upper right corner of each panel. The stacks are presented through a black line within a gray shade representing 1 σ -confidence bounds for the stacked amplitudes.

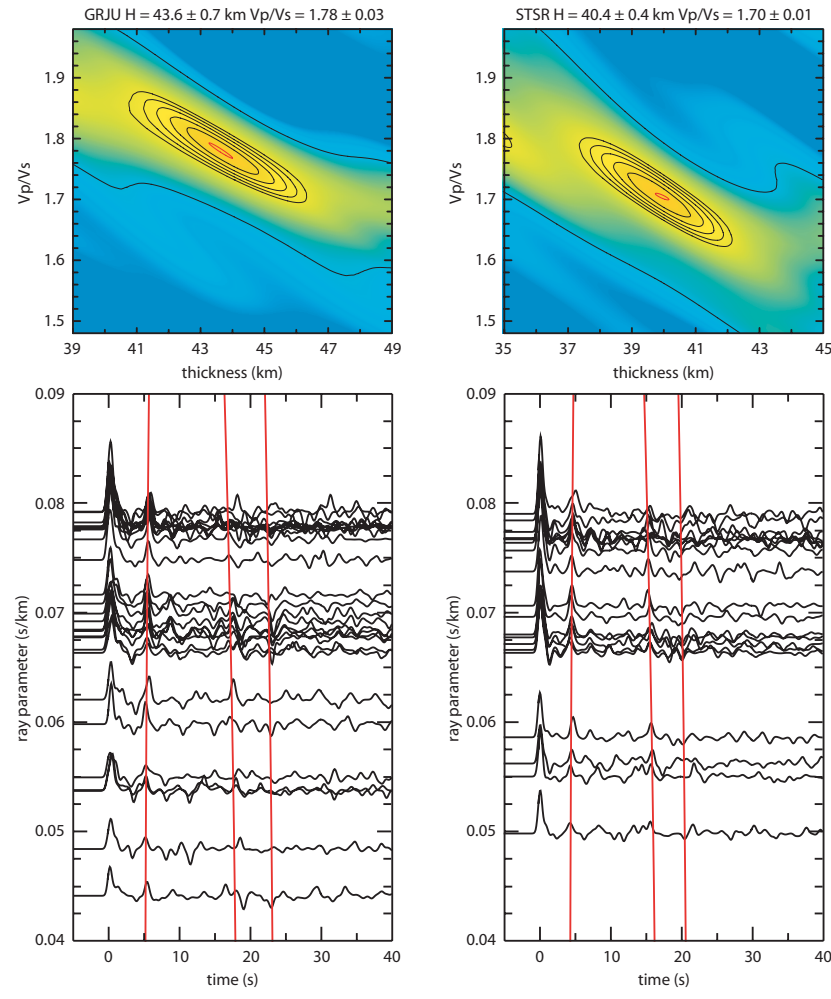


Figure 3: Sample $H\kappa$ stacking results for station STSR and GRJU. The top panels display the $H\kappa$ stacking surfaces, while the bottom panels display the corresponding radial receiver functions utilized during the stacking procedure, sorted by ray parameter. The thick, red line in the top panels is the 1σ -confidence ellipse from bootstrapping, and the thin, red lines in the bottom panels are the phase moveout curves for the Ps , $PpPs$ and $PpSs+PsPs$ phases associated to the maximum in the $H\kappa$ -stacking surface.

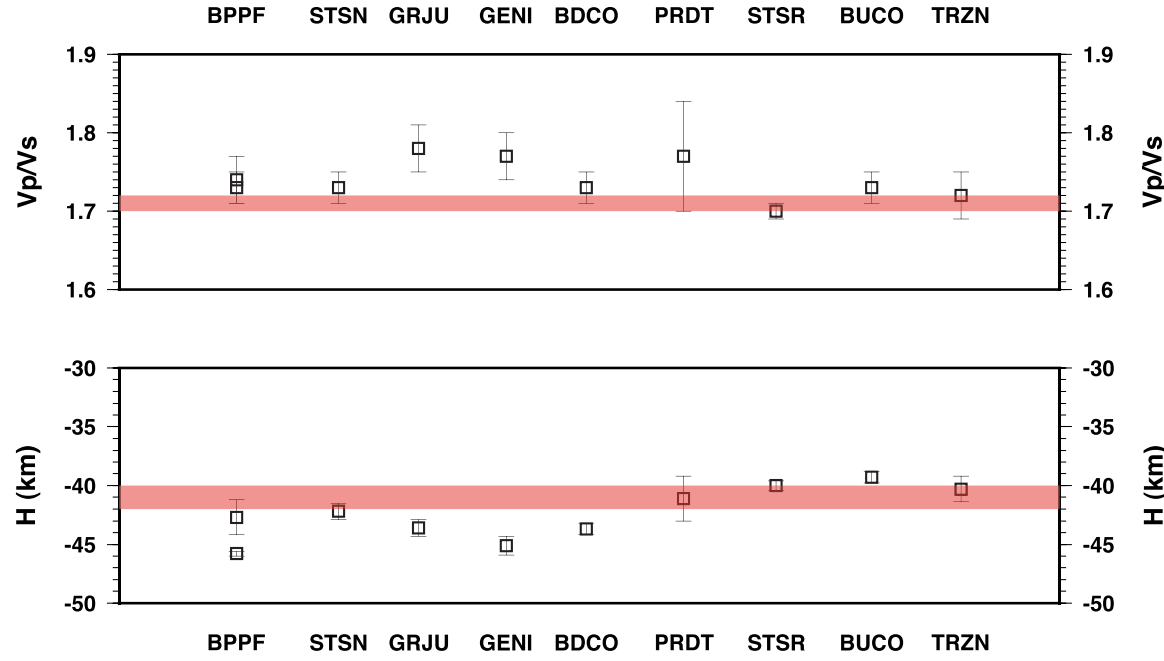


Figure 4: H - κ stacking results for V_p/V_s ratio (top) and crustal thickness (bottom) for all the stations in the Parnaíba basin. The vertical lines represent 2σ confidence bounds, while the red stripes mark the regions of 1.70-1.72 and 40-42 km variation in V_p/V_s ratio and crustal thickness, respectively. Note the thickening and increase in V_p/V_s ratio around stations GRJU, GENI, and BDCO.

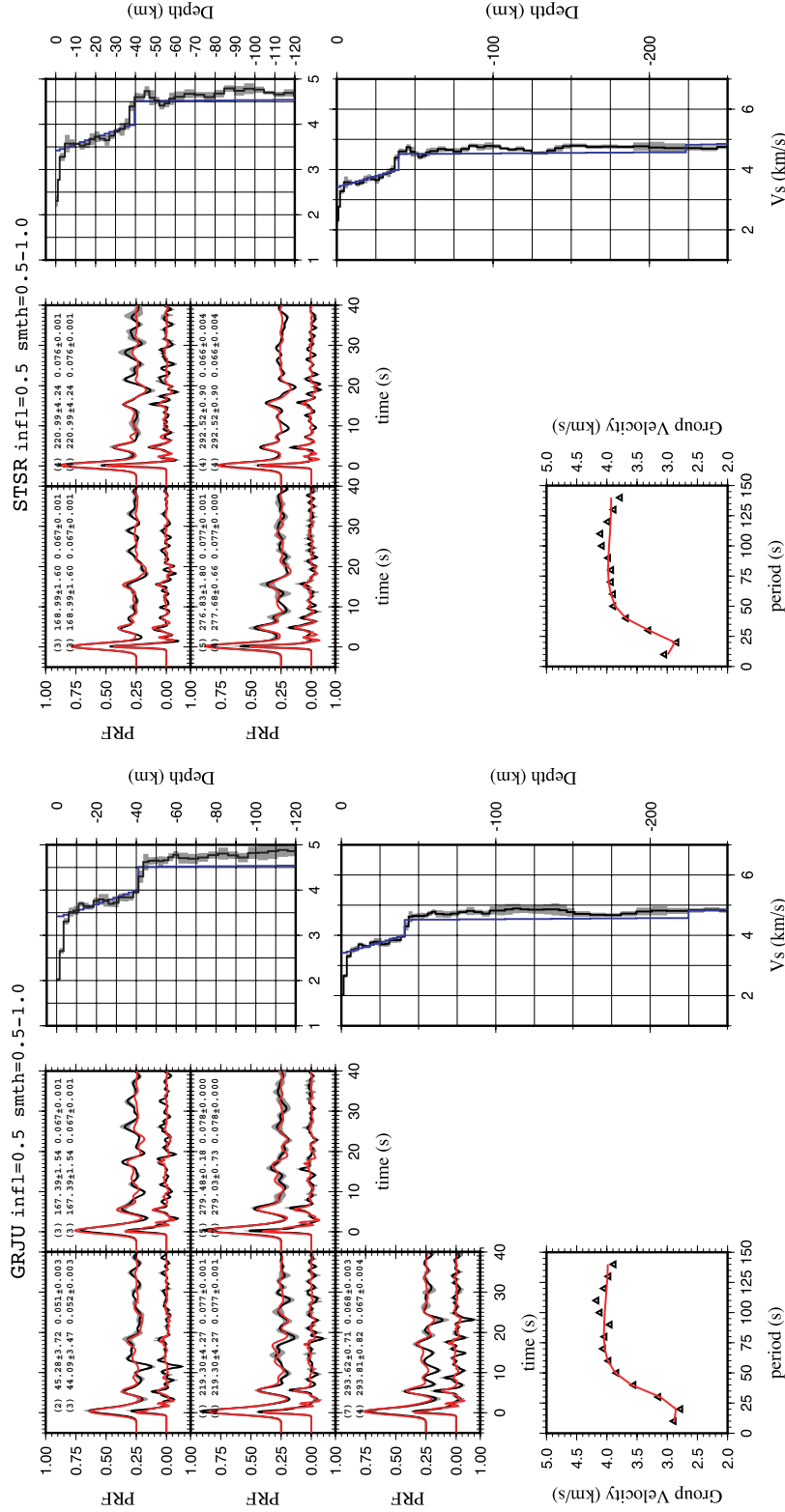


Figure 5: Joint inversion results for stations GRJU (left) and STSR (right). Comparison between observed (black) and predicted (red) receiver functions are shown in the upper-left panels, while comparison between observed (black triangles) and predicted (red line) group velocities are shown in the lower-left panels. The inverted (black line) and initial (blue line) S-velocity models are displayed in the right panels, along with the 2 σ -confidence bounds for the inverted velocities (grey band). The numbers next to the receiver function waveforms indicate the number of waveforms (n), the average back-azimuth (baz) and standard deviation ($sdbaz$), and the average ray parameter ($rayp$) and standard deviation ($sdrayp$), according to (n) $baz|pmstdbaz rayp\pm sdrayp$.

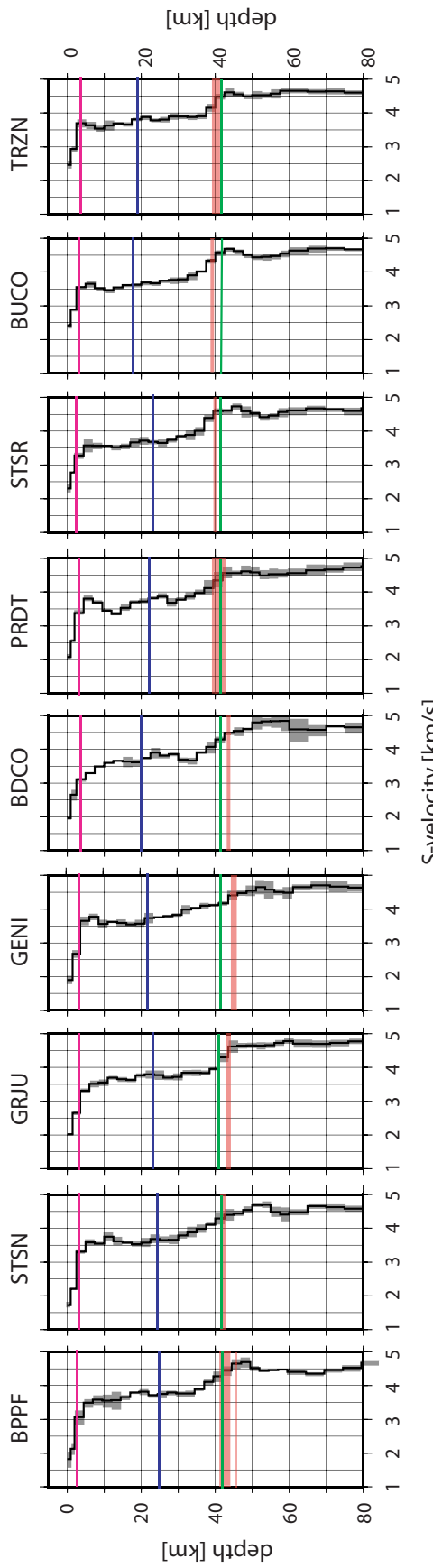


Figure 6: Joint inversion S-velocity models for each station along the profile, sorted according to station location. Inverted models are shown as black lines, with grey bands marking the 2σ -confidence bounds. $H-\kappa$ stacking results for crustal thickness are superimposed as red, transparent bands, for comparison. The main layer boundaries for the sediment-bedrock interface (purple), the upper-lower crust interface (blue) and crust-mangle boundary (green) from the seismic and gravity model of Tozer et al. (2017) have been superimposed to the velocity models. Note the thicker crust under stations GRIU, GENI, and BDCO, predicted by the joint inversion models.

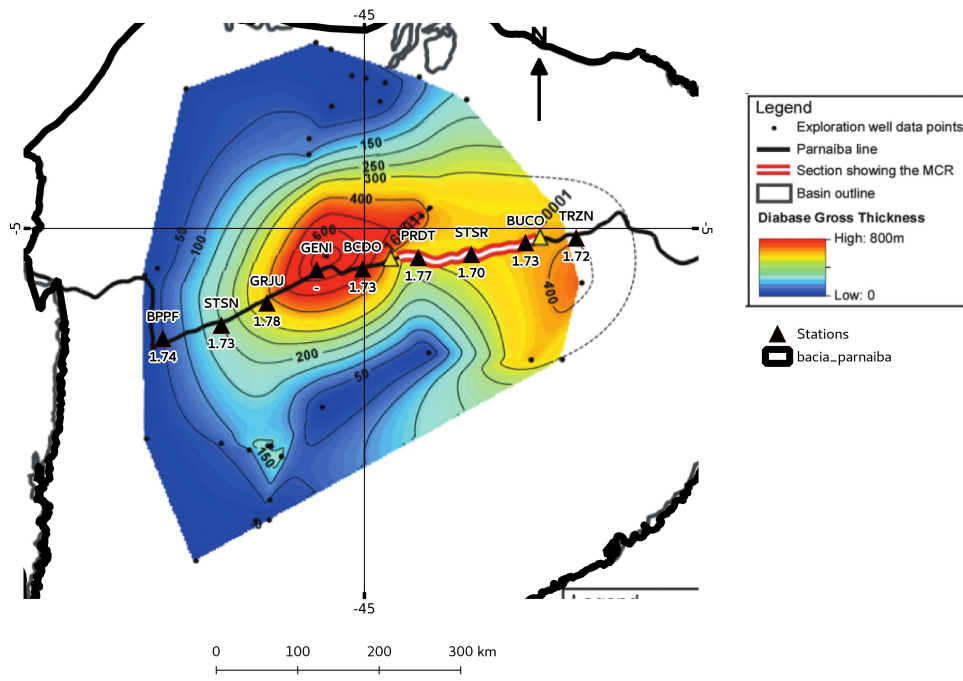


Figure 7: Cumulative isopach map for the Sardinha Formation with the location of our seismic stations superimposed. The Figure also displays the location of the seismic reflection line of Daly et al. (2014), along with the location of the Mid Crustal Reflector (MCR) imaged in their study. Note how stations GRJU, GENI, and BDCO are located on top of the thickest magmatic accumulation.